Integrated screens uncover a cell surface tumor suppressor gene *KIRREL* involved in Hippo pathway

Chao Wang[a,1], Xu Feng[a,1] [iD], Dan Su[a,1], Zhen Chen[a], Shimin Wang[a], Mengfan Tang[a], Min Huang[a], Litong Nie[a], Huimin Zhang[a], Siting Li[a], Ling Yin[a] [iD], Randy L. Johnson[b], Traver Hart[c], and Junjie Chen[a,2] [iD]

Cell surface proteins play essential roles in various biological processes and are highly related to cancer development. They also serve as important markers for cell identity and targets for pharmacological intervention. Despite their great potentials in biomedical research, comprehensive functional analysis of cell surface proteins remains scarce. Here, with a de novo designed library targeting cell surface proteins, we performed in vivo CRISPR screens to evaluate the effects of cell surface proteins on tumor survival and proliferation. We found that *Kirrel1* loss markedly promoted tumor growth in vivo. Moreover, KIRREL was significantly enriched in a separate CRISPR screen based on a specific Hippo pathway reporter. Further studies revealed that KIRREL binds directly to SAV1 to activate the Hippo tumor suppressor pathway. Together, our integrated screens reveal a cell surface tumor suppressor involved in the Hippo pathway and highlight the potential of these approaches in biomedical research.

Hippo | KIRREL | SAV1 | CRISPR | integrated screens

CRISPR screening is an advanced high-throughput strategy for revealing cancer vulnerabilities (1–3). Concerted efforts such as the Cancer Dependency Map (DepMap) have profiled cancer dependency in hundreds of cell lines in vitro, providing a rich resource of cancer driver genes and potential therapeutic targets (4–6). However, tumor growth and its microenvironment in vivo, such as cell–matrix interaction, cell–cell contact, and the immune microenvironment, cannot be faithfully reconstructed under in vitro culture conditions (7–9). Thus, xenograft-based CRISPR screens provide the advantage of more accurately recapitulating in vivo situations (10). In addition, CRISPR screens combined with specific reporters can provide comprehensive information about signaling transduction pathways (11). Therefore, we anticipate that the integration of different CRISPR-based functional screens will not only provide a comprehensive analysis of genes involved in tumor survival and proliferation but also reveal underlying mechanisms for further exploration.

The cell surface is the boundary that separates the cell from its environment. It is also the gateway for a cell to interact with its environment, including other cells and cell types. The cell surface is essential for many biological processes, including cell–cell interaction, cell adhesion, nutrition trafficking, and signal transduction (12). These important functions are coordinated by proteins at the cell surface that work as cell adhesion molecules, channels, transporters, receptors, and enzymes (13, 14). Because of the crucial roles of cell surface proteins in biological processes, many diseases such as cancer usually are accompanied with mutations and/or changes of the cell surface proteins. For example, mutations of the epidermal growth factor receptor are common in many types of cancers (15, 16). On the other hand, due to their accessibility, cell surface proteins are promising biomarkers and targets for pharmacological intervention. For instance, immune therapy targeting the cell surface protein programmed death-ligand 1 (PD-L1) has shown great promise in cancer treatment (17). Although great progress has been made in identifying cancer-related cell surface proteins, a comprehensive functional analysis of cell surface proteins involved in tumor growth or survival is lacking.

To comprehensively evaluate the functions of cell surface proteins in tumor survival and proliferation, we conducted CRISPR-based genetic screens both in vitro and in vivo with a de novo designed single-guide RNA (sgRNA) library targeting mouse cell surface proteins. Our screens not only recovered several key in vivo regulators critical for tumor survival, such as Pd-l1 and Cd47, but also identified *Kirrel* as a conserved tumor suppressor gene whose loss significantly promoted tumor growth in vivo. At the same time, we also recovered KIRREL as a Hippo signaling pathway component in our genome-wide CRISPR screen using a Hippo pathway–specific reporter.

KIRREL has been described as an immunoglobulin–superfamily cell adhesion molecule (18, 19). KIRREL is important in the organization and functional assembly of the

Significance

Cell surface proteins are essential for many biological processes. However, a comprehensive functional analysis of cell surface proteins involved in tumor growth and/or survival is missing. With a de novo designed cell surface sgRNA library targeting 1,147 cell–surface proteins, we provide an overview of the functions of these cell surface proteins in tumor growth through both in vitro and in vivo screens. Moreover, we identified a novel tumor suppressor gene, *KIRREL*. Furthermore, we showed that KIRREL activates the Hippo pathway by recruiting SAV1 to the cell membrane through a direct interaction between KIRREL and SAV1. Thus, our integrated CRISPR screens identified a tumor suppressor gene, *KIRREL*, that acts in the Hippo signaling pathway.

slit diaphragm, whose deletion causes the loss of glomerular filtration and results in podocyte foot process effacement (20). KIRREL is conserved from *Drosophila* to human. The *Drosophila* homolog of *KIRREL* is *roughest*, which is required for controlling cell numbers in the *Drosophila* retinal epithelium (21). The zebrafish KIRREL homolog Enph1 is a podocyte protein that is critical for maintaining renal function (22). However, the role of KIRREL in tumorigenesis is poorly understood.

The Hippo pathway is a tumor suppressor pathway that regulates cell proliferation and cell death (23). The Hippo pathway has been extensively studied in the past decades. The core of the Hippo pathway is composed of the kinase cascade Salvador 1 (SAV1)/Macrophage Stimulating 1/2 (MST1/2), MOB Kinase Activator 1A/B (MOB1A/B)/Large Tumor Suppressor Kinase 1/2 (LATS1/2), and the transcription complex Yes Associated Protein (YAP)/WW Domain Containing Transcription Regulator 1 (WWTR1)/TEA Domain Transcription Factor 1-4 (TEAD1-4) (24, 25). When the Hippo pathway is activated, MST1/2 phosphorylates LATS1/2, leading to LATS1/2 autophosphorylation and activation. LATS1/2 can further phosphorylate YAP/WWTR1, resulting in YAP/WWTR1 sequestration in cytoplasm and also their ubiquitination and degradation (25). YAP/WWTR1 is an important activator of transcription factor TEAD1-4, which regulates the expression of genes involved in cell proliferation, apoptosis, and differentiation. The Hippo pathway can be controlled by many upstream signals, such as G protein–coupled receptor (GPCR) signaling, cell–cell contact, and extracellular matrix stiffness (26–28). Other important Hippo pathway regulations include 14–3-3 proteins sequestering YAP in cytosol and Neurofibromin 2 (NF2) stabilizing LATS1/2 by inhibiting cullin-4-based RING-type (CRL4)/CUL4-associated factor 1 (DCAF1) complexes in nuclei (26, 29). In addition, spatial organization is important for the activation of the Hippo pathway. For example, LATS1/2 membrane association mediated by NF2 is important for LATS1/2 activities (30). Meanwhile, the SAV1 membrane association was also suggested to be essential for the activation of Hippo pathway, but its underlying mechanisms remain unclear.

Here, we identified *Kirrel* as a tumor suppressor gene through in vivo CRISPR screens. Our reporter-based whole-genome CRISPR screen indicated that KIRREL participates in the Hippo pathway. Moreover, our follow-up studies revealed that KIRREL binds directly to SAV1 and regulates SAV1 localization. These data demonstrate a role of KIRREL in tumorigenesis via regulating the Hippo pathway and further establish integrated CRISPR screening as an effective tool for defining the functions and the underlying mechanisms of genes involved in cancer development and other diseases.

Results

In vitro and in vivo CRISPR screens with a library targeting cell surface proteins.

To evaluate the functions of cell surface proteins in tumor survival and proliferation, we generated a CRISPR library targeting 1,157 cell surface genes (according to mass spectrometry [MS]–derived cell surface protein data [13]) and 98 control genes (49 essential and 49 nonessential genes), with four sgRNAs per gene (*SI Appendix*, Fig. S1A and Dataset S1). The quality of this ~5K size murine cell surface protein knockout (McspKO) library was then assessed by next-generation-sequencing (NGS) (*SI Appendix*, Fig. S1B), which confirmed an even distribution of sgRNAs. We then chose the B16 mouse melanoma model for our screens and infected B16 cells with this library (multiplicity of infection [MOI] < 0.3). After selection, cells were divided into three groups: in vitro culture, subcutaneous

tumor transplants into SCID nude mice, or subcutaneous tumor transplants into immunocompetent C57BL6 wild-type (WT) mice. For in vitro culture, cells were collected at day 10 (T10) or day 24 (T24) time points. The in vivo xenograft tumor samples were harvested at T24. The genomic DNA was then extracted from the cells/tissues, indexed with barcode primers, and subjected to NGS (Fig. 1A and Dataset S2). The raw reads, which were above 500-fold coverage in each group, were further analyzed (*SI Appendix*, Fig. S1C). As shown in Fig. 1B, the sgRNA distributions of three replicates from each group were clustered, suggesting the reliability of the screen results. Notably, the in vitro cultured groups and xenograft tumor groups were clustered separately, suggesting a difference between the in vitro and in vivo screens. We reasoned that a comparison of the screen results between the in vivo groups and the cultured cells could identify the genes important for in vivo tumor growth. Therefore, we compared the in vivo groups with in vitro groups via DrugZ analysis (Dataset S3). As shown in Fig. 1 C and D, we found several genes whose loss both led to tumor growth (growth-suppressing genes, green section) and retarded tumor growth (growth-promoting genes, red section). *Cd47* was recovered in the screen results from both nude and WT mice, consistent with Cd47's reported function, which is to protect cancer cells from macrophage-mediated phagocytosis (31). We also recovered *Cd274/Pd-l1* and *H2-T23*, two known genes involved in immune signaling (32, 33), as top hits in the screen result from C57BL6 mice but not from nude mice (Fig. 1 C and D). In addition, we compared the sgRNAs targeting each identified gene in each group and found the enhanced enrichment of these sgRNAs in the in vivo groups but not in the in vitro groups (*SI Appendix*, Fig. S1D). All these results not only validate the quality of the screens but also suggest the advantages of in vivo screens in capturing genes critical for tumor growth in vivo.

Among the genes whose loss advanced tumor growth, we noticed that *Kirrel* ranked as the top in both in vivo screens (Fig. 1 C and D). Meanwhile, all four sgRNAs targeting Kirrel were significantly enriched in the in vivo groups but not in the in vitro groups (Fig. 1E). The efficiency of sgRNAs targeting *Kirrel* was confirmed (*SI Appendix*, Fig. S1E). These results suggest that *Kirrel* functions as a tumor suppressor gene in vivo.

Validation of Kirrel tumor suppressor function in vivo.

We next performed cell competition experiments to validate the screen results. As shown in Fig. 2A, B16 cells were infected with control sgRNAs (cells labeled with red fluorescent protein [RFP]) and control or *Kirrel* sgRNAs (cells labeled with green fluorescent protein [GFP]). The mixed cells were cultured in vitro or subcutaneously transplanted into nude or C57BL6 mice. The tumor samples were harvested and digested into single cells. The cells from different groups were then analyzed with flow cytometry. As shown in Fig. 2 B and C, cells with sgRNAs targeting *Kirrel* (sgKirrel1/2) were enriched in both the in vivo groups (nude and C57BL6) but not in the in vitro groups (in vitro [T9] and in vitro [T21]), while cells with control sgRNAs were not enriched in any group. These results confirm the CRISPR screen results and support the in vivo tumor suppressor function of Kirrel.

Validation of KIRREL tumor suppressor function in human cancer cells.

Kirrel, which consists of five IgG-like domains, a transmembrane motif, and a cytosolic region, is a conserved protein from mice to humans (Fig. 3A). To verify whether the tumor suppression function of Kirrel is also conserved, we generated *KIRREL*-knockout (KO) HCT116 cells (Fig. 3B) and performed xenograft experiments in nude mice. As shown in Fig. 3C,
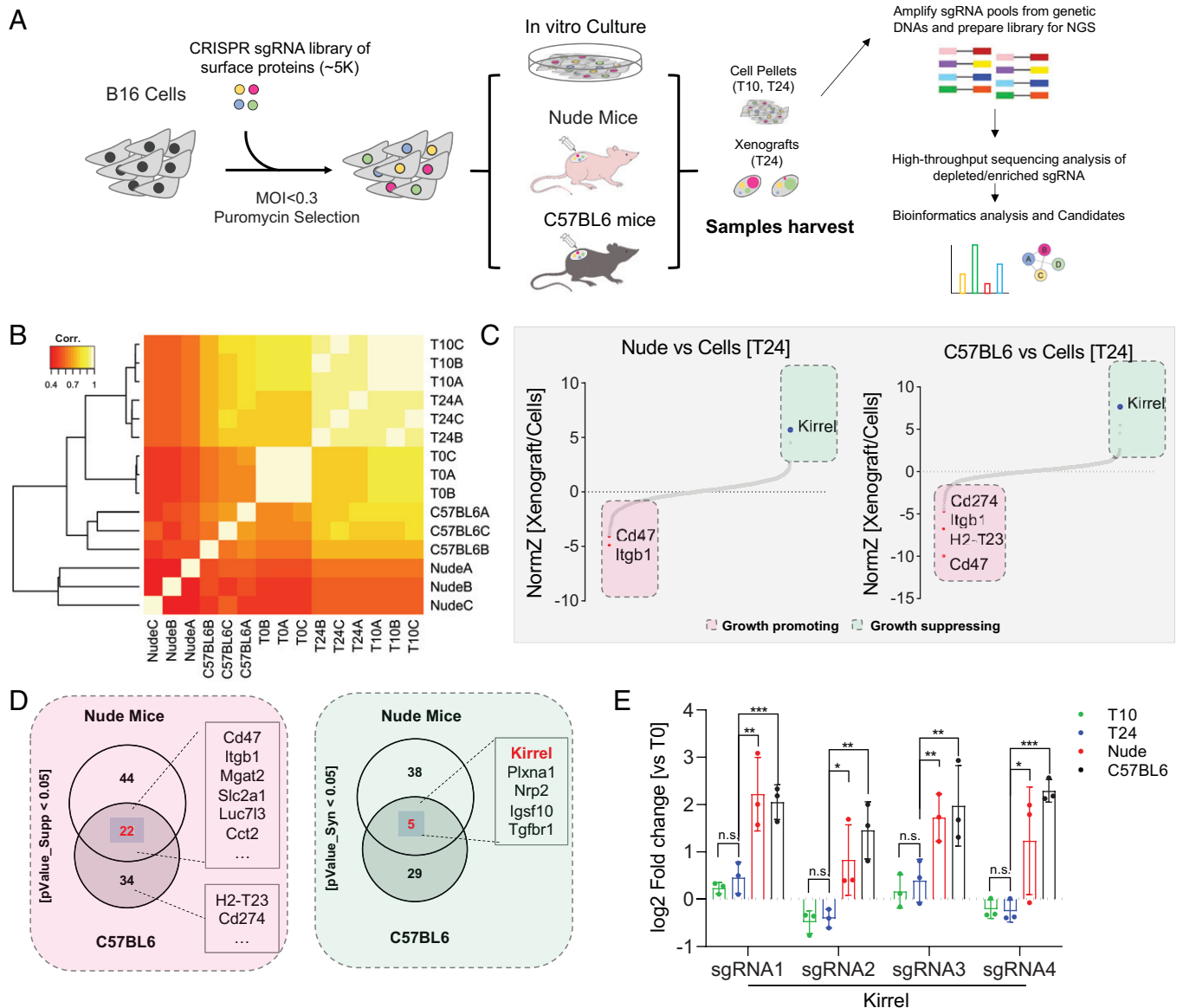
Fig. 1. Integrated CRISPR screens with a murine cell surface protein KO (McspKO) library identify *Kirrel* as a possible tumor suppressor gene. (*A*) Workflow of in vitro and in vivo screens with McspKO library for the identification of genes regulating tumor growth. A CRISPR library targeting murine cell surface genes was transduced into B16 mouse melanoma cells. Cells were then cultured in vitro or transplanted subcutaneously into nude (SCID) mice or C57BL6 mice. Tumor cells or tissues were harvested at day 10 (T10) and day 24 (T24), and sgRNAs were sequenced. (*B*) Pearson correlation coefficient of the normalized sgRNA read counts from indicated groups: freshly transduced cells (T0), in vitro cultured cells at T10 or T24, tumor samples from nude mice, and tumor samples from C57BL6 mice. Three replicates (marked as A, B, C) are shown. (*C*) DrugZ analysis of sgRNA abundance under each condition of the McspKO screens. The sgRNA read counts from in vivo groups (nude or C57BL6) were compared with the read counts from the in vitro group (cells [T24]). Positive NormZ scores indicate that the sgRNAs were enriched in the indicated in vivo group, suggesting that they target growth-suppressing genes. Negative NormZ scores indicate that the sgRNAs were depleted in the indicated in vivo group, suggesting that they target growth-promoting genes. The top growth-promoting genes (pValue_Supp < 0.05) or growth-suppressing genes (pValue_Syn < 0.05) were masked by red or green boxes, respectively. (*D*) Venn diagrams of common growth-suppressing or growth-promoting genes identified from the in vivo screen groups as outlined in (*C*). Kirrel, as the top growth suppressor gene, is marked in red. (*E*) The abundance of sgRNAs targeting Kirrel in different groups. The sgRNA read counts from the indicated groups were compared with the starting T0 group. Three replicates are shown, with the bars indicating mean ± SEM; n.s. = not significant; *$P < 0.05$, **$P < 0.01$, and ***$P < 0.001$, Student's *t* test.

compared to HCT116-WT control cells, the loss of KIRREL significantly promoted tumor growth in the transplanted model, suggesting that *Kirrel*/*KIRREL* is a conserved tumor suppressor gene from mice to humans.

KIRREL has high codependency with the Hippo tumor suppressor pathway. To investigate how KIRREL functions in tumor suppression, we first searched for codependency data from DepMap, which provides comprehensive information about genetic relationships between genes. We curated the 100 genes that are most correlated with *KIRREL* and performed gene ontology

(GO) enrichment analysis with these genes (Dataset S4). As shown in Fig. 3*D*, the actin regulation pathway (hsa048101), Hippo signaling pathway (hsa04392), and focal adhesion pathway (hsa04510) were enriched as the top *KIRREL*-related pathways. We further examined the individual corelated genes and found that genes involved in the Hippo tumor suppressor pathway showed a high positive correlation with *KIRREL* (e.g., NF2, ~0.47; LATS2, ~0.46), and genes involved in the actin regulation pathway displayed a negative correlation with *KIRREL* (e.g., PTK2, ~ −0.44; PKN2, ~ −0.42) (Fig. 3*E*). These data suggest that *KIRREL* is likely involved in these signaling pathways.
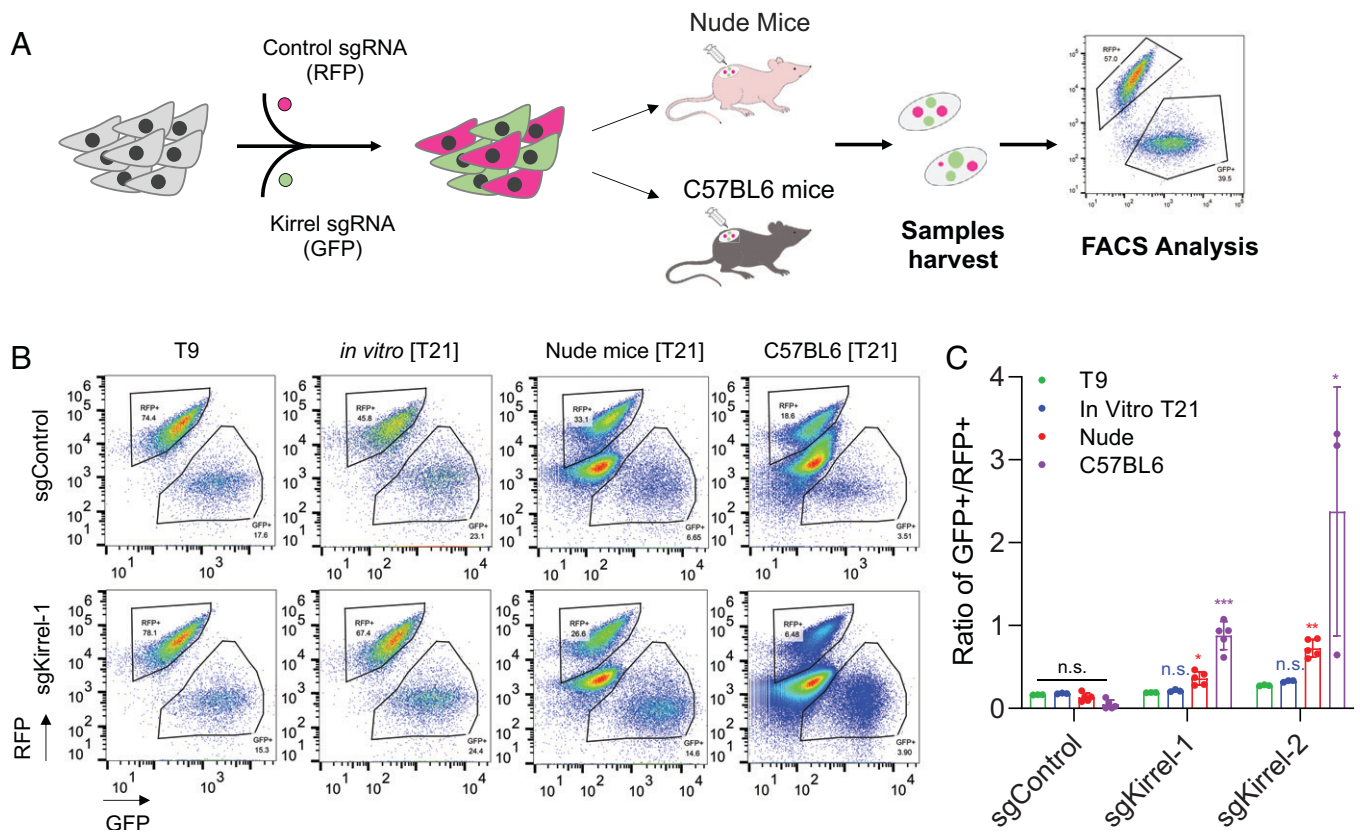
Fig. 2. Validation of Kirrel function with in vivo competition assays. (*A*) Workflow of in vivo competition assays. B16 cells expressing RFP or GFP were transduced with virus expressing the indicated sgRNAs. The cells were maintained in vitro or injected into nude mice or C57BL6 mice. Tumor cells of each group were collected, and flow cytometry analysis was performed. (*B*) Representative results of flow cytometry analysis for the experiment outlined in (*A*). (*C*) Quantification of relative percentages calculated from the flow cytometry analysis in (*B*). Data are shown as mean ± SEM; $n = 3$ mice per group. n.s. = not significant; *$P < 0.05$, **$P < 0.01$, and ***$P < 0.001$, Student t test, compared to the T0 group.

Reporter-based CRISPR screens identified KIRREL as a component of Hippo pathway. We also performed CRISPR screens to identify components of the Hippo pathway. We first constructed a Hippo pathway reporter cell line by expressing degradable RFP in human HEK293A cells (*SI Appendix,* Fig. S2A). The GTII reporter contains eight binding sites for the TEAD family of Hippo pathway transcription factors. Moreover, RFP was fused with a destabilization domain to subject the reporter to temporal control (34). In the absence of a stabilizer compound (trimethoprim [TMP]), RFP expression was undetectable because RFP is quickly degraded, while adding TMP to cells leads to RFP accumulation (*SI Appendix,* Fig. S2A). We then tested our reporter system by knocking out *NF2* or *LATS1/2* in the reporter HEK293A cells. As shown in *SI Appendix,* Fig. S2 *B–D*, the loss of *NF2* (*NF2*-KO) or *LATS1/2* (*LATS*-KO) significantly increased the RFP signals, validating this approach for the investigation of the Hippo pathway.

We then conducted genome-wide screens in HEK293A-WT, *NF2*-KO, and *LATS*-KO–GTII-dRFP cells, each in duplicate, with the Toronto Knockout (TKOv3) library. We simultaneously isolated cells with the highest 25% of RFP fluorescence (designated as TOP) and cells with the lowest 25% of RFP fluorescence (designated as BOT) by fluorescence-activated cell sorting (FACS), with ~8 million cells for each group. The genetic DNA was then extracted and sequenced. For each screen, sgRNA enrichment or depletion was calculated by comparing the BOT group with the corresponding TOP group by DrugZ analysis (Fig. 4A). Positive DrugZ scores meant that the sgRNAs were enriched in the TOP group, suggesting that the corresponding genes function in activating the Hippo tumor suppressor pathway. Negative DrugZ scores meant that the corresponding genes function in promoting

TEAD-dependent gene expression (Dataset S5). As shown in Fig. 4B, known Hippo pathway components such as NF2, Vestigial Like Family Member 4 (VGLL4), and LATS1/2 were identified as activators of the Hippo pathway, while WWTR1 was identified as essential for the Hippo pathway target gene expression, validating the reliability of our screen results. It is also of note that in the *NF2*-KO and *LATS*-KO groups, sgRNAs targeting these genes were not enriched either positively or negatively, further suggesting the reliability of our reporter-based screen results (Fig. 2 *B* and *C*).

Interestingly, we noticed that KIRREL was identified as an activator of the Hippo tumor suppressor pathway in the WT group. Moreover, as with NF2, the sgRNAs targeting *KIRREL* were not enriched in the *NF2*-KO or *LATS*-KO group (Fig. 4 *B* and *C*). These results, together with the previous codependency data derived from DepMap, suggest that KIRREL functions by activating the Hippo tumor suppressor pathway.

To validate our results, we knocked out *KIRREL* in HEK293A cells and performed an RNA-sequencing (RNA-seq) assay to compare the mRNA profiles between *KIRREL*-KO cells and WT cells (Dataset S6). As shown in Fig. 4D, Hippo pathway target genes were enriched among the up-regulating genes in the *KIRREL*-KO group. Moreover, the mRNA levels of all three classic Hippo pathway target genes (i.e., *CYR61*, *CTGF*, and *AMOTL2*) were significantly increased when *KIRREL* was knocked out (Fig. 4E). In addition, the protein levels of Angiomotin Like 2 (AMOTL2) and CYR61 were significantly increased in *KIRREL*-KO cells (Fig. 4F). Moreover, the loss of *KIRREL* in HEK293A cells induced CYR61 up-regulation at different cell confluences (*SI Appendix,* Fig. S2E). Consistently, the CYR61 protein level increased in HCT116 *KIRREL*-KO cells (*SI Appendix,* Fig. S2F). Using a
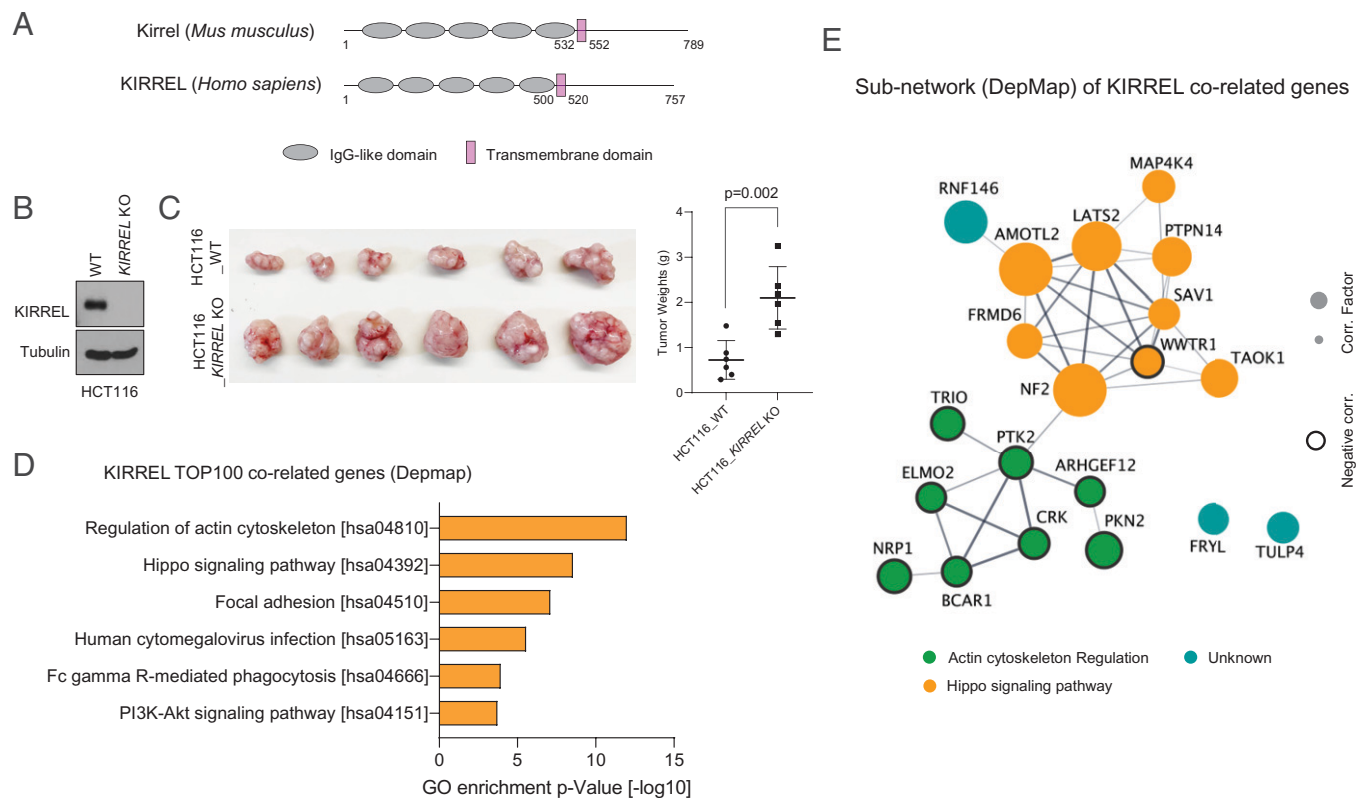
Fig. 3. Validation of KIRREL function in a human cancer cell line. (*A*) Schematic diagram of Kirrel (*Mus musculus*) and KIRREL (*Homo sapiens*). (*B*) Loss of *KIRREL* promoted the growth of HCT116 cells in vivo. *Left*, Cell lysates prepared from HCT116 cells or HCT116-*KIRREL* KO cells were blotted with the indicated antibodies. (*C*) WT or *KIRREL*-KO HCT116 cells were transplanted into nude mice. The tumors were harvested 4 wk after transplant. Quantification of tumor weights is shown in the right panel. Data are shown as mean ± SEM; *n* = 6 mice per group. *P* value was assessed by Student *t* test. (*D*) GO enrichment analysis of *KIRREL*-related genes. The top 100 genes codependent with *KIRREL* were downloaded from DepMap (https://depmap.org/portal/), and GO enrichment analysis was performed. (*E*) Hippo pathway genes and actin regulation genes were highly correlated with *KIRREL*. The curated *KIRREL*-related genes from (*D*) (correlation factor > 0.3 or < −0.3) were constructed into one network using the STRING database (https://string-db.org/).

GTII-luciferase reporter, we also found that *KIRREL*-KO significantly up-regulated the GTII–luciferase signals in both HCT116 and HEK293A cells (*SI Appendix*, Fig. S2*G*), suggesting that the loss of *KIRREL* led to inactivation of the Hippo pathway in different cell lines. In addition, as shown in *SI Appendix*, Fig. S2*H*, the CYR61 protein level was up-regulated and YAP phosphorylation was decreased in tumors derived from HCT116 *KIRREL*-KO cells when compared to those in tumors derived from control HCT116 WT cells, suggesting that *KIRREL*-KO also caused the inactivation of Hippo signaling in vivo. These data validated the RNA-seq results and suggested that KIRREL participates in the Hippo pathway.

We further generated *Kirrel* conditional KO mice (*Kirrel*^loxp/loxp) with LoxP-flanked *Kirrel1* exo 5–9 (*SI Appendix*, Fig. S2*I*) and *Kirrel*^−/− mouse embryonic fibroblasts (MEFs) via infection with the Cre retrovirus (*SI Appendix*, Fig. S2*J*). As shown in *SI Appendix*, Fig. S2*K*, the loss of *Kirrel* up-regulated the expression of the Hippo target gene *Cyr61* at high cell density. Together, these data suggest that KIRREL/Kirrel participates in the regulation of the Hippo pathway.

KIRREL participates in the Hippo pathway upstream of LATS1/2. To further evaluate the effects of KIRREL loss on the Hippo pathway, we determined the Hippo pathway signaling in control and *KIRREL*-KO cells. As shown in Fig. 4*G*, similar to those in *NF2* KO and *LATS1/2* double knock-out (DKO) cells, *KIRREL*-KO decreased pLATS1 and pYAP levels but did not affect the pMST1 level. Because a decreased pYAP level leads to YAP

nuclear localization, more nuclear YAP was observed in *KIRREL*-KO cells, similar to that observed in *NF2* KO and *LATS1/2* DKO cells (Fig. 4*H*). These data suggest that KIRREL may function upstream of LATS1/2 in regulating the Hippo pathway.

We also determined the effects of KIRREL loss in different cancer cell lines from various tissue/organs (i.e., lung: NCI-H1299, NCI-H460; bone: U2OS). As shown in *SI Appendix*, Fig. S3*A*, KIRREL protein levels were significantly decreased by *KIRREL* sgRNAs in all three cell lines. In addition, KIRREL loss decreased the pYAP level in H460 and U2OS cells. The expression of Hippo pathway target gene *CYR61* was up-regulated by KIRREL loss in H1299, H460, and U2OS cells. These data suggest that KIRREL regulates the Hippo pathway in multiple cancer cell lines. Consistently, KIRREL loss led to significant translocation of YAP into the nucleus in NCI-H1299, NCI-H460, and U2OS cells (*SI Appendix*, Fig. S3 *B* and *C*). All these data further confirmed the role of KIRREL in the regulation of the Hippo pathway.

Note that although the Hippo pathway was at least partially inactivated by KIRREL loss in the cell lines we tested, we only observed a modest advantage in cell proliferation in KIRREL-depleted U2OS cells when compared to that in WT cells (*SI Appendix*, Fig. S3*D*). Moreover, there was no significant difference in cell proliferation between HCT116 WT and *NF2* KO cells or between 293A WT, *NF2* KO, or *LATS* DKO cells (*SI Appendix*, Fig. S3 *E* and *F*). We speculate that any advantage in cell proliferation in these cell lines induced by the Hippo pathway inactivation may be difficult to detect under in vitro cell culture conditions.
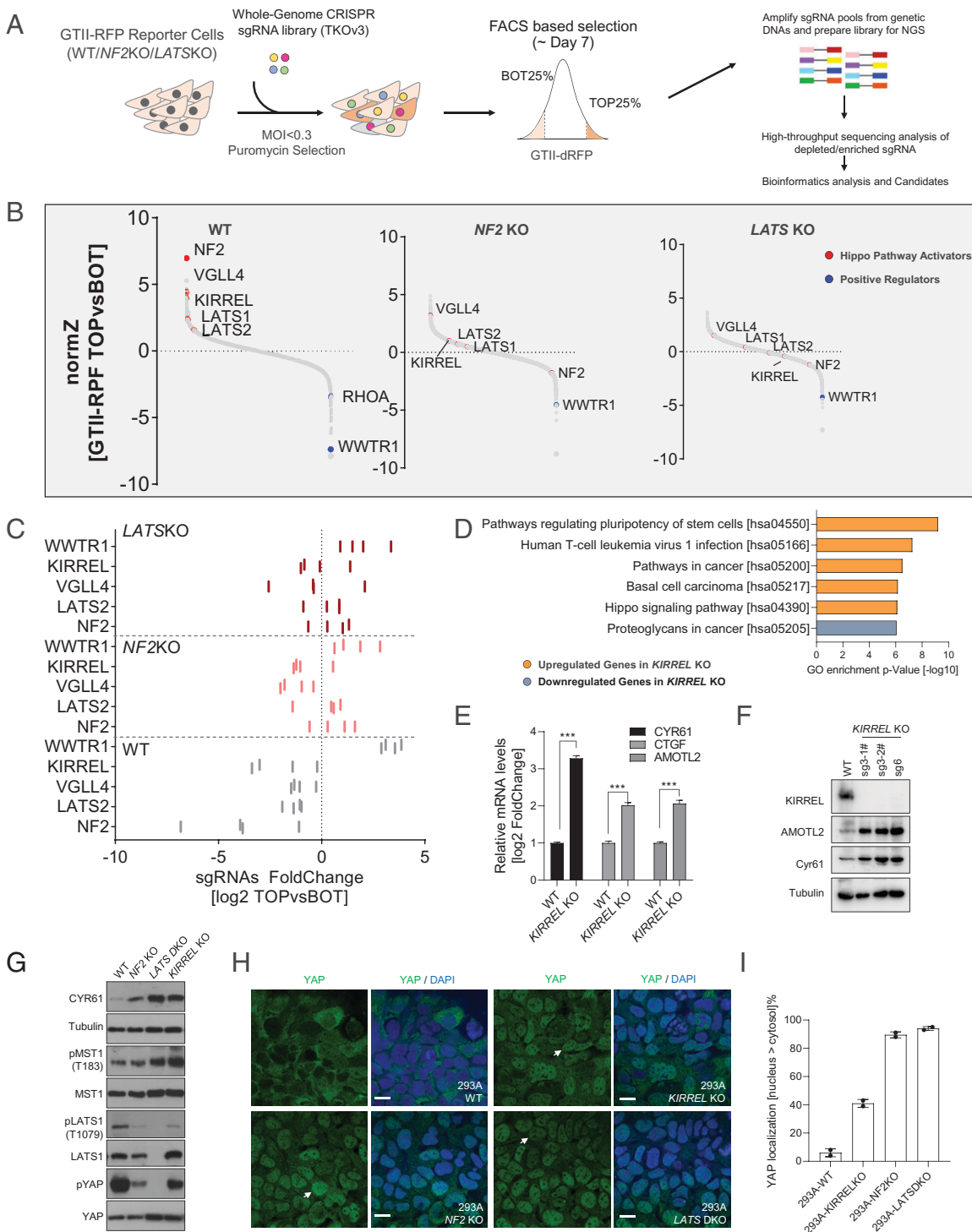
Fig. 4. Reporter-based CRISPR screens identify KIRREL as a Hippo pathway regulator. (*A*) Workflow of Hippo pathway reporter-based CRISPR screens. HEK293A WT, *NF2*-KO, and *LATS1/2*-KO (*LATS*-KO) cells with Hippo pathway reporter GTII-dRFP were constructed. These cells were then infected with the TKOv3 whole-genome sgRNA library. Seven days after puromycin selection, the indicated cells were sorted with flow cytometry. The cells with strong signals (top 25%, TOP) and cells with weak signals (bottom 25%, BOT) were selected. The sgRNAs from these cells were then sequenced and analyzed. (*B*) DrugZ analysis of sgRNA abundance between the TOP and BOT groups in reporter-based CRISPR screens. The sgRNA read counts from TOP populations were compared with BOT populations in the indicated groups. Positive NormZ scores indicate that the sgRNAs were enriched in the indicated TOP group, suggesting that they target positive regulators of the Hippo pathway. Negative NormZ scores indicate that the sgRNAs were depleted in the indicated BOT group, suggesting that they target negative regulators of the Hippo pathway. Several reported Hippo pathway regulators are marked in color (blue for positive regulators and red for negative regulators). (*C*) sgRNA enrichments or depletions for the curated genes. The fold changes of individual sgRNAs are listed. (*D*) GO enrichment analysis of genes with differential expression levels (log2 fold change > 1, FDR < 0.001) between WT and *KIRREL*-KO HEK293A cells. (*E*) Validation of the changed Hippo target genes from (*D*) by RT-PCR analysis. (*F*) Validation of the protein levels of the changed Hippo target genes from (*D*). Cell lysates from WT and *KIRREL*-KO HEK293A cells were collected and Western blotted with the indicated antibodies. (*G*) Validation of the Hippo pathway signaling in control and KO cells. Cell lysates from the indicated cells were blotted with the indicated antibodies. (*H*) Validation of YAP localization in control and KO cells. The indicated cells were plated at 2×10^6/well in 6-well plate. The next day, the cells were fixed and immunostained with YAP antibody and DAPI. Representative images are shown from duplicate experiments. The white arrows indicate the cells with dominant YAP localization (nucleus > cytosol) (Scale bar, 10 μM). (*I*) Quantification of percentages of cells with dominant YAP nuclear localization (nucleus > cytosol) in (*G*); duplicates are shown.

KIRREL interacts with the Hippo pathway component SAV1.
To uncover how KIRREL is involved in the Hippo pathway, we performed tandem affinity purification (TAP) and proximity labeling followed by MS assays to search for KIRREL-associated proteins (Fig. 5A and Dataset S7). Through both methods, we identified SAV1, MST1, and MST2 of the Hippo pathway among the KIRREL-interacting proteins (Fig. 5B). We further validated our MS results by coimmunoprecipitation experiments. As shown in Fig. 5C, among the tested Hippo pathway components, only SAV1 showed a strong interaction with KIRREL, suggesting that KIRREL participates in the Hippo pathway through binding to SAV1.

We then mapped the interaction between KIRREL and SAV1 by generating constructs encoding different truncated forms of KIRREL and SAV1. As shown in Fig. 5 D–F, the SAV1-binding region was mapped to residues 600 to 757 of KIRREL, while the loss of residues 1 to 120 of SAV1, but not the WW domains or the SARAH domain, significantly decreased the interaction between these two proteins. These results suggest that the interaction between KIRREL and SAV1 may be mediated by residues 600 to 757 in KIRREL and residues 1 to 120 in SAV1.

KIRREL promotes the spatial regulation and function of SAV1 in the Hippo pathway. As shown in Fig. 6A and SI Appendix, Fig. S4A, KIRREL is localized in membrane that is marked by ZO-1 or pan-cadherin. KIRREL-KO diminished the membrane KIRREL signals (Fig. 6A and SI Appendix, Fig. S4A), which further confirmed the membrane localization of KIRREL. Consistently, KIRREL protein was enriched in the membrane fraction of 293A cells (SI Appendix, Fig. S4B). In addition, as shown in SI Appendix, Fig. S4C, KIRREL binds to itself, suggesting a homotypic interaction, which is consistent with a previous report (35). Moreover, the loss of KIRREL in one cell led to the mislocalization of KIRREL in the adherent cell (SI Appendix, Fig. S4D), suggesting that the homotypic interaction is important for KIRREL localization.

We hypothesized that KIRREL may regulate SAV1 through its membrane localization. Thus, we examined the localization of SAV1 in cells with SAV1 coexpressed with KIRREL-WT or a KIRREL-Δ600–757 mutant. As shown in SI Appendix, Fig. S4E, coexpression with KIRREL localized SAV1 to the cell membrane while coexpression with the KIRREL-Δ600–757 mutant failed to do so. Consistently, the overexpression of KIRREL-WT, but not the KIRREL-Δ600–757 mutant, increased the SAV1 protein level in the membrane fraction (Fig. 6B). All these data suggest the spatial regulation of SAV1 by KIRREL.

Furthermore, while KIRREL-KO led to the decrease of pLATS and pYAP levels in 293A cells (Figs. 4G and 6C), the expression of KIRREL-WT, but not the expression of the KIRREL-Δ600–757 mutant, rescued these phenotypes (Fig. 6C). Consistently, the up-regulation of Hippo pathway target genes (i.e., CYR61 and AMOTL2) in KIRREL-KO cells was suppressed by the expression of KIRREL-WT but not by that of the KIRREL-Δ600–757 mutant (Fig. 6D). Although we did not observe any significant change in cell proliferation in 293A cells with inactivation of the Hippo pathway in 2-dimensional (2D) culture, LATS DKO promoted colony formation in 3-dimensional (3D) matrigel culture, as revealed by the larger colony sizes in LATS DKO cells (Fig. 6 E and F). Similar to LATS DKO, KIRREL-KO also promoted 3D matrigel colony formation in 293A cells, which could be suppressed by the re-expression of KIRREL-WT but not by the expression of the KIRREL-Δ600–757 mutant (Fig. 6 E and F). All these data suggest that KIRREL interacts with SAV1, leads

to SAV1 membrane localization, and promotes the function of SAV1 in the Hippo pathway (SI Appendix, Fig. S4F).

Discussion

In this study, we performed in vitro and in vivo CRISPR screens with a de novo designed sgRNA library targeting cell surface proteins to evaluate their functions in tumor growth. Besides the genes known to regulate tumor growth in vivo, we identified a conserved tumor suppressor gene, Kirrel/KIRREL. In addition, the DepMap codependency data and our Hippo pathway reporter-based CRISPR screen results further suggest that KIRREL participates in the Hippo tumor suppressor pathway. Moreover, we showed that KIRREL activates the Hippo pathway by recruiting SAV1 to the membrane through a direct interaction between KIRREL and SAV1. Thus, we identified a tumor suppressor gene that acts upstream of the Hippo pathway through integrated CRISPR screens.

The cell surface is the gateway for the cell to interact with its microenvironment and therefore plays essential roles in many cellular processes, including nutrition exchange, cell–cell or cell–extracellular matrix contact, and signal transduction (14). Cell surface proteins are the "executors" of cell surface functions. Although several families of cell surface proteins have been studied extensively, including GPCRs, receptor–tyrosine kinases, and ion channels, a comprehensive evaluation of cell surface proteins has not yet been conducted. The advances in CRISPR-based functional screens make it practical to perform large-scale and comprehensive analysis of cell surface proteins. Here we generated a CRISPR library containing ~5K sgRNAs targeting 1,157 cell surface genes compiled based on experimental evidence (13). Although our study only evaluated the functions of these cell surface proteins in tumor growth, this cell surface sgRNA library can be used to analyze many other processes, including but not limited to nutrition trafficking, signal transduction, and immune evasion.

CRISPR screens have been widely used in identifying cancer drivers and cancer vulnerabilities. Efforts such as DepMap have characterized cancer dependency in hundreds of cancer cell lines, providing valuable resources for cancer research. However, CRISPR screens based on an in vitro culture system may not properly represent the in vivo environment, such as interaction with stromal cells or the immune system (7, 11). In this study, in parallel with in vitro culture, we performed screens in immunodeficient and immunocompetent mice. This design allowed us to compare different groups to evaluate genes that are required in different systems. For example, Cd274/Pd-l1 could only be identified in screens with immunocompetent mice, which is consistent with its role as an adaptive immune checkpoint. On the other hand, Cd47 showed up in screens with both immunocompetent and immunodeficient mice, which is consistent with its role in preventing cells from macrophage-mediated phagocytosis. These data further suggest the advantages of in vivo screens in studying immuno-related genes.

Moreover, CRISPR screening using an in vivo xenograft model is a powerful tool to reveal drivers that are essential for tumor growth. In this study, Kirrel/KIRREL was identified as a tumor suppressor gene by in vivo screens. Interestingly, a previous study using CRISPR screens in a 3D cancer model also identified KIRREL as a cancer driver in NCI-H23 and NCI-H1975 cells (7), which further supports our findings. Note that although it was reported that the inactivation of tumor suppressor pathways, such as the Hippo pathway, could lead to advantages in cell proliferation in vitro in 2D culture (25), we did not observe any significant change in cell proliferation caused by NF2 KO or LATS1/2
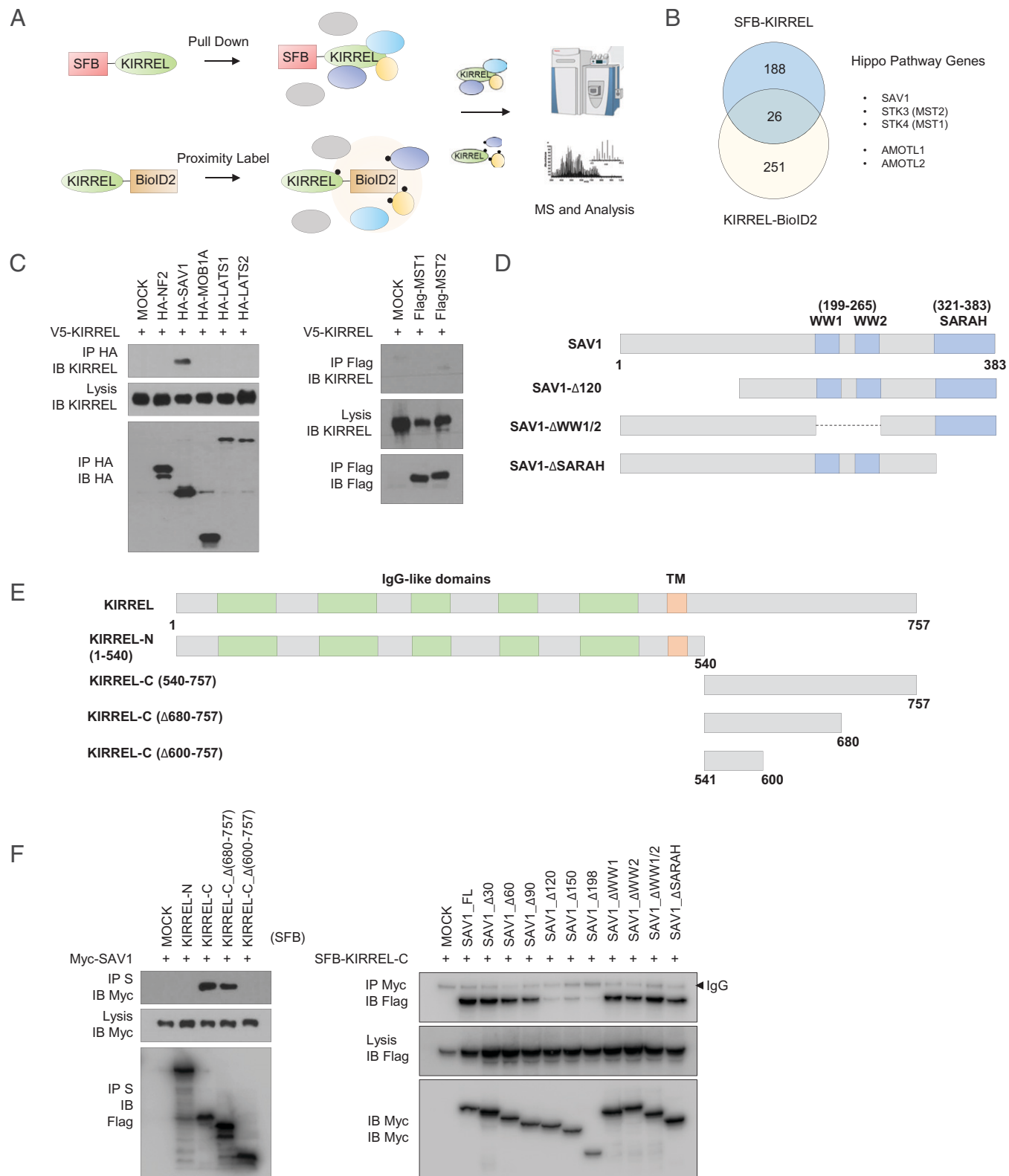
Fig. 5. KIRREL interacts with SAV1. (*A*) Workflow of TAP and proximity labeling together with MS assays to profile KIRREL interactome. S protein-Flag-Streptavidin binding peptide (SFB)-tagged KIRREL or BioID2-fused KIRREL was expressed in HEK293T cells. For TAP samples, cell lysates were purified in a 2-step method (streptavidin beads and S-protein beads). For proximity-labeling samples, biotin was added into the medium 8 h before harvesting cells, and the cell lysates were then purified with streptavidin beads. The purified samples were then analyzed by MS. (*B*) Overlapping high-confidence KIRREL-related proteins from both methods. (*C*) Coimmunoprecipitation (IP) assays identified that KIRREL binds to SAV1. The plasmids expressing Hippo pathway components and KIRREL were cotransfected into HEK293T cells. Cells were harvested 48 h after transfection, and coimmunoprecipitation was performed. The samples were then subjected to Western blotting (IB) with the indicated antibodies. (*D*) Schematic diagram of SAV1 protein and truncated SAV1 forms used in the following experiments. Blue marks the known domains of SAV1. (*E*) Schematic diagram of KIRREL protein and truncated KIRREL forms used in the following experiments. Green marked the Ig-G like domains of KIRREL. Orange marks the transmembrane (TM) domain of KIRREL. (*F*) Coimmunoprecipitation assays were used to map the binding domains in KIRREL and SAV1. The plasmids expressing full-length (FL) or truncated forms of SAV1 or KIRREL were transfected into HEK293T cells. Cells were harvested 48 h after transfection, and coimmunoprecipitation was performed. The samples were then subjected to Western blotting with the indicated antibodies.
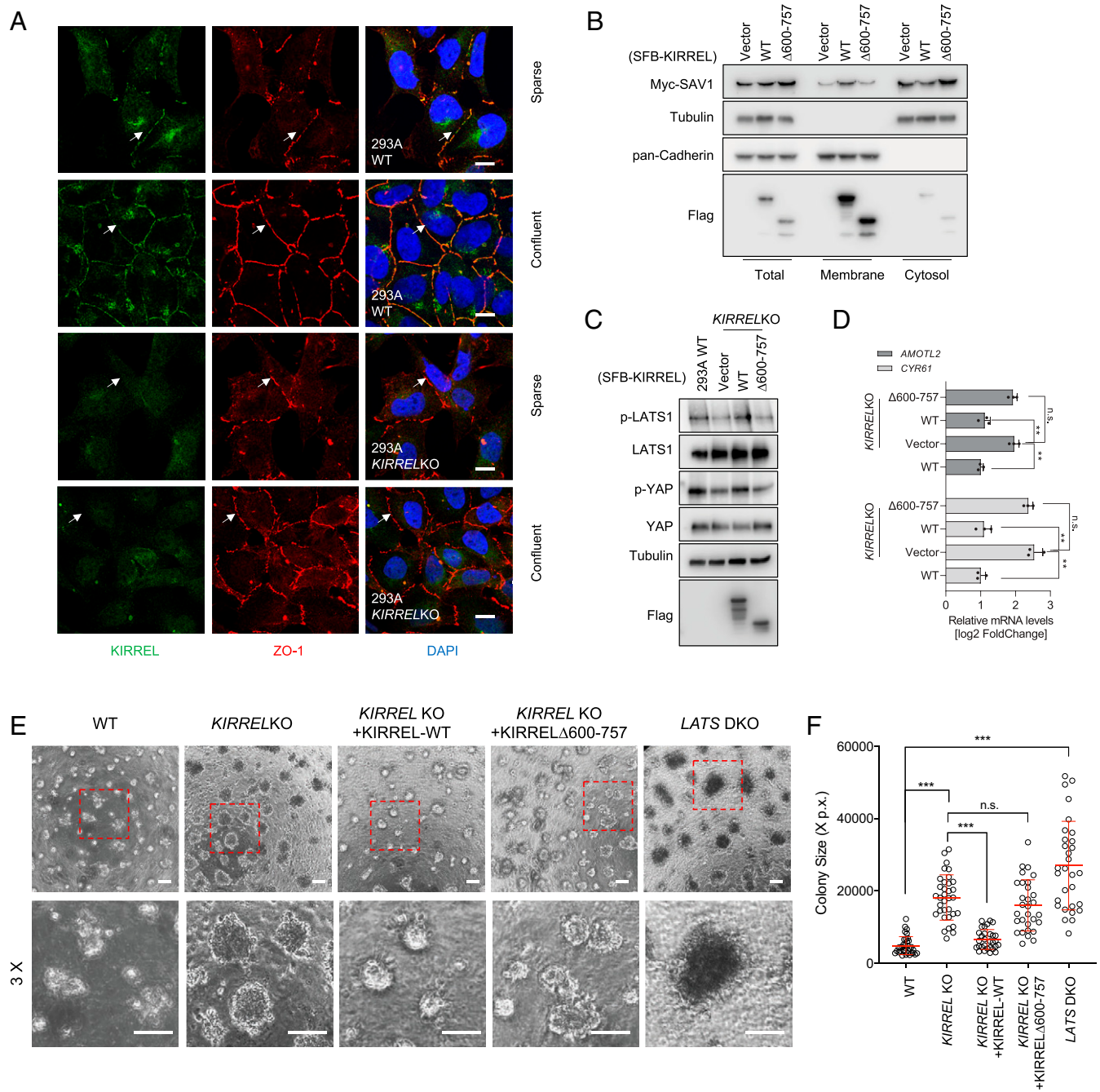
Fig. 6. KIRREL localizes in membrane and activates the Hippo pathway through SAV1. (*A*) Immunofluorescence staining shows membrane localization of KIRREL. The indicated cells at different densities were stained with the indicated antibodies. ZO-1 marks the cell membrane and cell–cell junction. Arrows indicate cell membrane as revealed by anti–ZO-1 staining (Scale bar, 5 μM). (*B*) KIRREL localized SAV1 to the membrane fraction. HEK293T cells were transfected with plasmids encoding the Myc-SAV1 and the indicated KIRREL-WT or truncated form. Then 48 h after transfection, cells were harvested and different cell fractions were separated. Western blots were then performed with the indicated antibodies. (*C*) The HEK293A WT cells, *KIRREL* KO cells and *KIRREL* KO cells expressing the KIRREL-WT or Δ600–757 form were harvested. The cell lysates were blotted with the indicated antibodies. (*D*) RT-PCR analysis of the Hippo pathway target genes *AMOTL2* and *CYR61* mRNA levels from the same cells described in (*C*). Three replicates are shown, with the bars indicating mean ± SD; n.s. = not significant; **P < 0.01, Student's t test. (*E*) The 3D matrigel culture of the same cells described in (*C*). We plated 2 × 10⁴ cells/well in 48-well plates with a mixture of medium and growth factor reduced matrigel (ratio 1:1). Photos were taken after 10 d of culture. The regions of the dashed boxes were enlarged and are shown in the lower panel. Representative results are shown (Scale bar, 100 μM). (*F*) Quantification of 3D colony sizes of each group in (*F*); n.s.= not significant; ***P < 0.001, Student's t test.

DKO. We speculate that the cell proliferation rate may already be high under in vitro 2D culture conditions, which makes it difficult to detect any further increase in cell proliferation. Nevertheless, our results showed that the inactivation of the Hippo pathway led to a growth advantage when we used the in vivo xenograft model and the in vitro 3D culture model, which further supports the advantage of in vivo screens for the identification of genes that may influence tumor growth in vivo.

Codependency data from DepMap are a rich resource to search for genetic relationships, which could be used not only to recover known genetic interactions (e.g., TSC1-TSC2) but also to reveal new genetic interactions (e.g., AMBRA1-RB1) (5, 36). Codependency data, together with our Hippo pathway reporter-based genetic screen results, suggested a role of KIRREL in the Hippo pathway. Follow-up experiments reported in this study further demonstrated that KIRREL participates in the Hippo

pathway through regulating SAV1. These data together reveal the advantages of integrated CRISPR screens, e.g., in vitro, in vivo, database, and reporter-based screens, in uncovering new genes and the mechanisms underlying their functions.

While this study was being revised, a study reported that KIRREL regulates the Hippo signaling pathway through SAV1 (37), which agrees with our findings. Moreover, we have provided additional data to support the potential tumor suppressor function of KIRREL. We evaluated the functions of a large number of cell surface proteins in regulating cell growth via an unbiased approach, which unequivocally revealed the growth suppression function of Kirrel in vivo. In addition, we showed that KIRREL loss led to growth advantage using an in vivo xenograft model and in vitro 3D culture model. We also demonstrated that YAP nuclear localization was significantly increased by KIRREL loss in multiple cell lines. Moreover, phosphorylation levels of LATS1 and YAP, but not of MST1, were decreased in *KIRREL*-KO cells. Finally, we generated *Kirrel* conditional KO mice and confirmed that *Kirrel* loss led to the inactivation of the Hippo pathway in MEF cells. These data further support our working hypothesis that KIRREL regulates the Hippo tumor suppression pathway.

The Hippo pathway is a classic tumor suppressor pathway that has been carefully studied. This pathway is stringently regulated by many factors, such as GPCR signaling, cell contact, and the extracellular matrix (24). The Hippo pathway is also under spatial regulation. For example, 14–3-3 proteins control the Hippo pathway activity through sequestering YAP in cytosol, while NF2 can stabilize LATS1/2 proteins through inhibiting CRL4-DCAF1 complexes in the nucleus (29). It has also been reported that NF2 relocated LATS1/2 to the membrane and activated its activities directly (30). However, the spatial regulator of SAV1/MST is still unknown. Here, we identified KIRREL as the transmembrane regulator of the Hippo pathway through SAV1, which suggests a mechanism by which SAV1 is recruited to the membrane to initiate the Hippo pathway. Moreover, because KIRREL is a transmembrane protein, it will be interesting to further determine whether it mediates cell–cell contact inhibition through Hippo and other pathways and whether it functions in organ size control during development.

Materials and Methods

Cell lines, plasmids, and antibodies. B16, HEK293A, and HEK293T cells were purchased from ATCC and cultured in Dulbecco's modified Eagle medium supplemented with 10% fetal calf serum. HCT116 cells were purchased from ATCC and cultured in McCoy's 5A medium supplemented with 10% fetal calf serum. U2OS, H460, and H1299 cells were purchased from ATCC and cultured in RPMI1640 medium supplemented with 10% fetal calf serum.

CRISPR (McspKO) library design and construction. We designed a CRISPR library containing 4,993 sgRNAs targeting 1,157 previously reported cell surface genes (13), 49 core essential genes, and 49 nonessential genes. Each oligo (77 nt) contained 20 nt sgRNA, a 5′ universal flanking sequence (CTTGTGGAAAGGACGAAA CACCG), and a 3′ flanking sequence (GTTTTAGAGCTAGAAATAGCAAGTTAAAATAAGG). The oligo library was synthesized by CustomArray Inc. The sequences of the sgRNAs are provided in Dataset S1. The McspKO library was amplified and cloned into lentiCRISPRv2 plasmids using Gibson Assembly Reaction Master Mix (NEB, E2611S).

Integrated screens with McspKO library. The McspKO library was transfected into HEK293T cells with the packaging vector psPAX2, the envelope vector pMD2.G, and the X-treme Gene transfection reagent (Roche). The virus-containing media were collected 24 h after transfection, centrifuged at 1,500 rpm for 5 min, and frozen for subsequent sgRNA screens. For sgRNA screening, 20 million B16 cells were infected with lentiviruses encoding the McspKO library at a low MOI ratio (< 0.3). Twenty-four hours after infection, the medium was replaced with fresh medium containing puromycin (2 μg/mL). After selection, cells were split

into different groups containing 5 million cells each, passaged every 3 d. In vivo screens were performed in C57BL/6 mice (Jackson Laboratory, 000664) or nude mice (Jackson Laboratory, 001803) strains. For each replicate, the infected cells were transplanted into 10 different 6- to 8-wk-old female mice, with ~2 million cells per injection. At day 24, tumors were harvested and digested overnight at 55 °C with lysis buffer (10 mM Tris [pH 8.0; Boston Bioproducts BBT-80], 10 mM EDTA [Boston Bioproducts BM-150], 0.5% SDS [Invitrogen 15553035], and proteinase K [Invitrogen 25530-049] to 0.2 mg/mL). Genomic DNA was isolated via phenol/chloroform (Thermo Fisher Scientific 15593-049) extraction and used in PCRs to generate libraries for NGS on an Illumina NextSeq. 500 system to determine sgRNA abundance. DrugZ analysis was used to calculate the difference between different groups.

In vivo competition experiments. B16 cells expressing RFP or GFP were infected with lentivirus encoding control sgRNAs or *Kirrel* sgRNAs, respectively. B16 cells were then mixed at a ratio of 4:1 (control sgRNA–infected cells:*Kirrel* sgRNA–infected cells). The mixed cells were then cultured in vitro or injected into nude mice or C57BL6 mice. At the indicated time points, tumors or cells were collected and digested, and flow cytometry was performed.

Hippo pathway reporter-based CRISPR screens. The TKOv3 library was transfected into HEK293T cells with the packaging vector psPAX2, the envelope vector pMD2.G, and the X-treme Gene transfection reagent. The virus-containing media were collected 24 h after transfection, centrifuged at 1,500 rpm for 5 min, and frozen for subsequent sgRNA screens. For sgRNA screening, 120 million reporter cells (293A-GTII-dRFP, *NF2*-KO–GTII-dRFP, *LATS*-KO–GTII-dRFP) were infected with lentiviruses encoding the TKOv3 library at a low MOI ratio (< 0.3). Twenty-four hours after infection, the medium was replaced with fresh medium containing puromycin (2 μg/mL). After selection, cells were split into different groups containing ~20 million cells each, passaged every 3 d, and maintained at 200-fold coverage. At day 5 after selection, 1 mM TMP was added into the medium for 48 h. Cells were then trypsinized and selected with flow cytometry according to the RFP signal. Genomic DNA was extracted from cell pellets using the QIAamp Blood Maxi Kit (Qiagen), precipitated using ethanol and sodium chloride, and resuspended in Buffer EB (10 mM Tris–HCl [pH 7.5]). PCR was used to amplify sgRNA inserts; primers harboring Illumina TruSeq adapters with i5 and i7 barcodes were used, and the resulting libraries were sequenced on an Illumina NextSeq. 500 system. The BAGEL algorithm (https://github.com/hart-lab/bagel) was used to calculate essentiality scores. DrugZ analysis (https://github.com/hart-lab/drugz) was used to calculate the difference between different groups.

Generation of KO cells. KO cells were generated using pLentiCRISPRv2. Cells were transiently transfected with the indicated plasmids and selected using puromycin (2 μg/mL). Single cells were then plated into 96-well plates. After 10 d, clones were picked and checked with the indicated antibodies using Western blotting.

Antibodies. The antibodies used in this study were as follows: mouse anti-KIRREL (sc-373787, Santa Cruz Biotechnology), rabbit anti-CYR61 (39382S, Cell Signaling Technology), rabbit anti-AMOTL2 (HPA063027, Sigma-Aldrich), mouse anti–alpha-tubulin (T6199, Sigma-Aldrich), anti–phospho-YAP (Ser127) (4911S, Cell Signaling Technology), anti-phospho-LATS1 (Thr1079) (8654S, Cell Signaling Technology), anti-phospho-MST1(Thr183) (49332S, Cell Signaling Technology), anti-vinculin (V9264, Sigma-Aldrich), anti-HA (H3663, Sigma-Aldrich), anti-V5 (R960-25, Thermo Fisher), and anti-FLAG (F1804, Sigma-Aldrich).

sgRNAs and short hairpin RNAs. The sgRNAs and short hairpin RNAs (shRNAs) used in this study were as follows:
    human *KIRREL* sgRNA-3#: TGTCTCATAGCGACTCTCGT;
    human *KIRREL* sgRNA-6#: TGAGCCACAGACGGTGCAGG;
    mouse *Kirrel* sgRNA-1#: CGAGATGGGACACAGCAGGA;
    mouse *Kirrel* sgRNA-2#: GAGGCCCTGGCCCATACCCA;
    human *KIRREL* shRNA-1#: AGTTCTCGTAGGACAGCTG (RHS4430-200232175, Horizon).

Western blotting. Cells were lysed in NETN buffer (20 mM Tris [pH 7.6], 1 mM ethylenediaminetetraacetic acid, 1% Nonidet P-40, 150 mM NaCl) supplemented with protease-inhibitor mixture tablets (Roche). Proteins were separated by sodium

dodecyl sulfate polyacrylamide gel electrophoresis (SDS-PAGE), transferred to membranes, and immunoblotted with antibodies as indicated in the figures.

Immunoprecipitation, proximity labeling, and MS. Expression plasmids were transfected into HEK293T suspension cells with polyethyleneimine. Cells were harvested 64 h after transfection, and pellets were directly lysed with NETN buffer (20 mM Tris—HCl [pH 7.5], 150 mM NaCl, 10% glycerol, 0.5% Nonidet P-40, 10 mM NaF, 1 mM phenylmethylsulfonyl fluoride [PMSF], 1 μg/mL leupeptin, 1 μg/mL aprotinin). The lysates were ultracentrifuged at 15,000 rpm for 15 min, and then the supernatant was incubated with streptavidin beads for 3 to 4 h at 4 °C. The beads were washed 4 times with NETN buffer and eluted with NETN containing 2 mg/mL biotin. The elution was then incubated with S-protein beads at 2 °C. The beads were washed 4 times with NETN buffer and eluted with NETN containing 2 mg/mL biotin. The elution was then again incubated with S-protein beads for 2 h. Subsequently, S-protein beads were washed, and the complexes were eluted and analyzed by SDS-PAGE and MS.

For proximity-labeling proteins, cells expressing BioID2-tagged genes were treated with 50 mM biotin for 18 h and then harvested. Pellets of cells were then subjected to lysis and centrifugation as described above. The supernatant was incubated with streptavidin-conjugated beads (Thermo Fisher Scientific) for 3 to 4 h at 4 °C. Then the beads were washed with NETN buffer, and the complexes were eluted and analyzed by SDS-PAGE and MS.

For mapping the interactions between proteins, modified NETN buffer (20 mM Tris—HCl [pH 7.5], 250 mM NaCl, 10% glycerol, 0.5% Nonidet P-40, 10 mM NaF, 1 mM PMSF, 1 μg/mL leupeptin, 1 μg/mL aprotinin, 25 U/mL benzonase, and 100 μg/mL RNase A) was used to eliminate any possible chromatin-mediated interactions.

Cell proliferation assay. Cells were grown at 0.5×10^6/well in 6-well plates and were passaged at ratio 1:4 every 3 days. Cell numbers were counted with an automated cell counter (TC20, Bio-Rad) and calculated accordingly.

Genetically engineered mouse model and MEFs. The mice with LoxP-flanked *Kirrel* exon 5–9 were generated in C57BL/6J background by the Cyagen Co. The MEFs were isolated from the *Kirrel* $^{loxp/loxp}$ embryos at day 16.

For the generation of retroviruses expressing Cre, pCL-ECO (NBP2-29540; NOVUS Biologicals) and pBabe-Puro (#1764; Addgene)/pBabe-Cre-Puro (gifted from Boyi Gan Lab) were transfected in HEK293T cells. Retroviruses were collected 48 h after transfection. The *Kirrel* $^{floxp/floxp}$ cells were then infected with the indicated viruses for 24 h and selected with puromycin (2 μg/mL). The cells were then harvested, and the genomic DNA was examined by PCR with the indicated primers. The correct knock-out cells were used for the experiments.

Primers for mice and MEF genotyping were as following: PCR 1# Forward: TTATCCCAGGGCATTGAAGTAGG; PCR 1# Reverse: CAGACCCTTACCTCCTCGTTTAG; PCR 2# Forward: GGCAGCCCTTGGTGTGTCC; PCR 2# Reverse: CCAGGCTGGCCTCGAACTCAG.

3D matrigel culture. The growth factor–reduced matrigel matrix was plated in 48-well cell plates ahead of time. The indicated cells (2×10^4/well) were grown in a mixture of medium and growth factor–reduced matrigel matrix at a 1:1 ratio. The colonies were analyzed after 10 d of growth in matrigel, and at least 2 replicates were performed.

Immunofluorescence staining analysis. Cells were grown on coverslips for 24 h before treatment. After the indicated treatment, cells were fixed in 4% para-formaldehyde and permeabilized with PBS with 0.5% Triton X-100. Then cells were incubated with primary antibodies diluted in PBST-BSA for 1 h at room temperature. After 3 washes with PBS, fluorescently labeled secondary antibodies in PBST-BSA were added for 1 h. Cells were then washed in PBS with Hoechst stain (1:10 000). Slides were imaged at 40× magnification on a Leica microscope.

RNA-seq and data analysis. HEK293A WT or *KIRREL*-KO cells were collected, and total RNA was extracted using an RNeasy Mini Kit (Qiagen; 74104)

according to the manufacturer's instructions. The library was prepared using an Illumina TruSeq Stranded Total RNA Library Prep Kit, including rRNA depletion and sequencing using a NextSEq. 550 system to generate 75 bp paired ends.

For RNA-seq data analysis, reads were adapter-trimmed and preprocessed with Cutadapt software (version 1.15) for quality control and data filtering. Genome mapping was conducted using STAR (version 2.5.3a) and the human reference genome (GRCh38). Gene abundance was measured by HTseq-count uniquely mapped reads number with default parameters and using the ENSEMBL v83 annotations. Only genes with > 5 reads in at least one sample were retained. The raw read counts of retained genes were submitted for differential expression analysis by DESeq2 software. The resulting *P* values were adjusted by the Benjamini and Hochberg approach to control for the false discovery rate (FDR). Genes with fold change > 1.35 and FDR < 0.05 were considered as differentially expressed genes. Standard gene set enrichment analysis was performed with a hypergeometric test using the RDAVID WebService (v1.19.0).

RNA isolation and RT-qPCR. Total RNA was prepared using TRIzol (Invitrogen) and reverse-transcribed using the PrimeScript RT Reagent Kit with the genomic DNA Eraser (Takara, RR047A). The qPCR reactions were run in an ABI Q6 RT-PCR instrument. Levels of DHPS mRNA were detected by the TaqMan MicroRNA assay (ABI Scientific) and normalized by β-actin mRNA. The primers used in this study were as follows: (β-actin forward: CACCATTGGCAATGAGCGGTTC; β-actin reverse: AGGTCTTTGCGGATGTCCACGT; AMOTL2 forward: AGTGAGCGACAAACAGCAGACG; AMOTL2 reverse: ATCTCTGCTCCCGTGTTTGGCA; CYR61 forward: GGAAAAGGCAGC TCACTGAAGC; CYR61 reverse: GGAGATACCAGTTCCACAGGTC).

Subcellular fractionation. HEK293A cells were transfected with the indicated plasmids. Next, 48 h after transfection, cells were harvested and subcellular fractionation was performed using Mem-PER plus a membrane protein extraction kit (Thermo Scientific) according to the manufacturer's instructions.

Luciferase reporter assay. Constructs encoding the indicated proteins were cotransfected into HEK293T cells along with 8XGTII-luciferase together with Renilla luciferase as the internal control. After 48 h, cells were lysed using a passive lysis buffer (Promega), and luciferase assays were performed using a dual-luciferase assay kit (Promega). The assay results were quantified using a Monolight 3010 luminometer (Becton Dickinson).

Statistical analysis. Statistical analyses were performed using GraphPad Prism software (version 8.0). All of the statistical methods used are described in the main text. Each experiment was repeated 3 times if not specifically mentioned in the text. Differences between groups were analyzed using the Student's *t* test, unless otherwise noted. A *P* value < 0.05 was considered statistically significant.

1. L. A. Gilbert et al., Genome-scale CRISPR-mediated control of gene repression and activation. *Cell* **159**, 647–661 (2014).
2. T. Hart et al., High-resolution CRISPR screens reveal fitness genes and genotype-specific cancer liabilities. *Cell* **163**, 1515–1526 (2015).
3. O. Shalem et al., Genome-scale CRISPR-Cas9 knockout screening in human cells. *Science* **343**, 84–87 (2014).
4. E. M. Chan et al., WRN helicase is a synthetic lethal target in microsatellite unstable cancers. *Nature* **568**, 551–556 (2019).
5. M. Ghandi et al., Next-generation characterization of the cancer cell line encyclopedia. *Nature* **569**, 503–508 (2019).
6. A. Tsherniak et al., Defining a cancer dependency map. *Cell* **170**, 564–576.e16 (2017).

7. K. Han *et al.*, CRISPR screens in cancer spheroids identify 3D growth-specific vulnerabilities. *Nature* **580**, 136–141 (2020).
8. S. K. Loganathan *et al.*, Rare driver mutations in head and neck squamous cell carcinomas converge on NOTCH signaling. *Science* **367**, 1264–1269 (2020).
9. M. Saigi, J. J. Alburquerque-Bejar, M. Sanchez-Cespedes, Determinants of immunological evasion and immunocheckpoint inhibition response in non-small cell lung cancer: The genetic front. *Oncogene* **38**, 5921–5932 (2019).
10. I. P. Winters, C. W. Murray, M. M. Winslow, Towards quantitative and multiplexed in vivo functional cancer genomics. *Nat. Rev. Genet.* **19**, 741–755 (2018).
11. K. A. Lawson *et al.*, Functional genomic landscape of cancer-intrinsic evasion of killing by T cells. *Nature* **586**, 120–126 (2020).
12. M. S. Almén, K. J. Nordström, R. Fredriksson, H. B. Schiöth, Mapping the human membrane proteome: A majority of the human membrane proteins can be classified according to function and evolutionary origin. *BMC Biol.* **7**, 50 (2009).
13. D. Bausch-Fluck *et al.*, A mass spectrometric-derived cell surface protein atlas. *PLoS One* **10**, e0121314 (2015).
14. D. Bausch-Fluck *et al.*, The in silico human surfaceome. *Proc. Natl. Acad. Sci. U.S.A.* **115**, E10988–E10997 (2018).
15. S. V. Sharma, D. W. Bell, J. Settleman, D. A. Haber, Epidermal growth factor receptor mutations in lung cancer. *Nat. Rev. Cancer* **7**, 169–181 (2007).
16. T. J. Lynch *et al.*, Activating mutations in the epidermal growth factor receptor underlying responsiveness of non-small-cell lung cancer to gefitinib. *N. Engl. J. Med.* **350**, 2129–2139 (2004).
17. M. W. LaFleur, Y. Muroyama, C. G. Drake, A. H. Sharpe, Inhibitors of the PD-1 pathway in tumor therapy. *J. Immunol.* **200**, 375–383 (2018).
18. P. J. Durcan, N. Al-Shanti, C. E. Stewart, Identification and characterization of novel Kirrel isoform during myogenesis. *Physiol. Rep.* **1**, e00044 (2013).
19. L. Sellin *et al.*, NEPH1 defines a novel family of podocin interacting proteins. *FASEB J.* **17**, 115–117 (2003).
20. D. B. Donoviel *et al.*, Proteinuria and perinatal lethality in mice lacking NEPH1, a novel protein with homology to NEPHRIN. *Mol. Cell. Biol.* **21**, 4829–4836 (2001).
21. T. Wolff, D. F. Ready, Cell death in normal and rough eye mutants of Drosophila. *Development* **113**, 825–839 (1991).
22. E. Arif *et al.*, Slit diaphragm protein Neph1 and its signaling: A novel therapeutic target for protection of podocytes against glomerular injury. *J. Biol. Chem.* **289**, 9502–9518 (2014).
23. Y. Zheng, D. Pan, The Hippo signaling pathway in development and disease. *Dev. Cell* **50**, 264–282 (2019).
24. F. X. Yu, K. L. Guan, The Hippo pathway: Regulators and regulations. *Genes Dev.* **27**, 355–371 (2013).
25. S. W. Plouffe *et al.*, Characterization of Hippo pathway components by gene inactivation. *Mol. Cell* **64**, 993–1008 (2016).
26. B. Zhao *et al.*, Inactivation of YAP oncoprotein by the Hippo pathway is involved in cell contact inhibition and tissue growth control. *Genes Dev.* **21**, 2747–2761 (2007).
27. F. X. Yu *et al.*, Regulation of the Hippo-YAP pathway by G-protein-coupled receptor signaling. *Cell* **150**, 780–791 (2012).
28. Z. Meng *et al.*, RAP2 mediates mechanoresponses of the Hippo pathway. *Nature* **560**, 655–660 (2018).
29. W. Li *et al.*, Merlin/NF2 suppresses tumorigenesis by inhibiting the E3 ubiquitin ligase CRL4(DCAF1) in the nucleus. *Cell* **140**, 477–490 (2010).
30. F. Yin *et al.*, Spatial organization of Hippo signaling at the plasma membrane mediated by the tumor suppressor Merlin/NF2. *Cell* **154**, 1342–1355 (2013).
31. Y. Kojima *et al.*, CD47-blocking antibodies restore phagocytosis and prevent atherosclerosis. *Nature* **536**, 86–90 (2016).
32. Y. Iwai *et al.*, Involvement of PD-L1 on tumor cells in the escape from host immune system and tumor immunotherapy by PD-L1 blockade. *Proc. Natl. Acad. Sci. U.S.A.* **99**, 12293–12297 (2002).
33. V. M. Braud, D. S. J. Allan, A. J. McMichael, Functions of nonclassical MHC and non-MHC-encoded class I molecules. *Curr. Opin. Immunol.* **11**, 100–108 (1999).
34. E. E. Er *et al.*, Pericyte-like spreading by disseminated cancer cells activates YAP and MRTF for metastatic colonization. *Nat. Cell Biol.* **20**, 966–978 (2018).
35. P. Gerke, T. B. Huber, L. Sellin, T. Benzing, G. Walz, Homodimerization and heterodimerization of the glomerular podocyte proteins nephrin and NEPH1. *J. Am. Soc. Nephrol.* **14**, 918–926 (2003).
36. A. C. Chaikovsky *et al.*, The AMBRA1 E3 ligase adaptor regulates the stability of cyclin D. *Nature* **592**, 794–798 (2021).
37. A. Paul *et al.*, Cell adhesion molecule KIRREL1 is a feedback regulator of Hippo signaling recruiting SAV1 to cell-cell contact sites. *Nat. Commun.* **13**, 930 (2022).